Atmos. Meas. Tech., 9, 2721–2734, 2016
www.atmos-meas-tech.net/9/2721/2016/
doi:10.5194/amt-9-2721-2016

Atmospheric Measurement Techniques
Open Access
EGU

A miniDOAS instrument optimised for ammonia field measurements

Jörg Sintermann[1,a], Klaus Dietrich[2], Christoph Häni[3], Michael Bell[4], Markus Jocher[1], and Albrecht Neftel[1]

[1]Agroscope – Institute for Sustainability Science, Zurich, Switzerland
[2]Interstate University of Applied Sciences Buchs NTB, Buchs, Switzerland
[3]Bern University of Applied Sciences, School of Agricultural, Forest and Food Sciences HAFL, Zollikofen, Switzerland
[4]INRA, UMR 1069 SAS, Rennes, France
[a]now at: Office of Waste, Water, Energy and Air, Canton of Zurich, Zurich, Switzerland

Correspondence to: Jörg Sintermann (sintermann@gmx.ch) and Albrecht Neftel (neftel_a@bluewin.ch)

Received: 20 November 2015 – Published in Atmos. Meas. Tech. Discuss.: 19 January 2016
Revised: 17 May 2016 – Accepted: 27 May 2016 – Published: 29 June 2016

Abstract. We present a differential optical absorption spectroscopy (DOAS) instrument, called "miniDOAS", optimised for optical open-path field-measurements of ambient ammonia (NH_3) alongside nitrogen oxide (NO) and sulfur dioxide (SO_2). The instrument is a further development of the miniDOAS presented by Volten et al. (2012). We use a temperature-controlled spectrometer, a deuterium light source and a modified optical arrangement. The system was set up in a robust, field-deployable, temperature-regulated housing. For the evaluation of light spectra we use a new high-pass filter routine based upon robust baseline extraction with local regression. Multiple linear regression including terms of an autoregressive–moving-average model is used to determine concentrations. For NH_3 the random uncertainty is about 1.4 % of the concentration, and not better than 0.2 µg m^{-3}. Potential biases for the slope of the calibration are given by the precision of the differential absorption cross sections (±3 %) and for the offset by the precision of the estimation of concentration offsets (c_{ref}) introduced by the reference spectrum I_{ref}. Comparisons of miniDOAS measurements to those by NH_3 acid trap devices showed good agreement. The miniDOAS can be flexibly used for a wide range of field trials, such as micrometeorological NH_3 flux measurements with approaches based upon horizontal or vertical concentration differences. Results from such applications covering concentration dynamics of less than one up to several hundreds of µg m^{-3} are presented.

1 Introduction

Accurate, high-time-resolution measurements of NH_3 for ambient concentration monitoring, source apportionments and flux measurements are still a challenge due to the stickiness of this molecule and its interactions with inlet or instrument surfaces, water and aerosol particles (Parrish and Fehsenfeld, 2000). Differential optical absorption spectroscopy (DOAS) with open-path arrangement offers a contact-free, in situ way to determine ambient NH_3, which features narrow absorption lines in the UV range between 200 and 230 nm. In this wavelength range, concentration determination by DOAS over path lengths up to 100 m is possible (Edner et al., 1993; Gall et al., 1991; Mount et al., 2002), but instrument performance can pose a challenge for scientific trials (Emmenegger et al., 2004; Mennen et al., 1996; Neftel et al., 1990). Volten et al. (2012) developed a "miniDOAS", for continuous, high-time-resolution NH_3 (combined with NO and SO_2) measurements. This system has recently been implemented in the Dutch air-monitoring network. It has been designed for the purpose of concentration monitoring, where the system can be set up in the protected environment of a monitoring station with solid installation, climate regulation and easy access to the miniDOAS. Collaborating with the developer group (RIVM, Bilthoven, the Netherlands), we further developed this miniDOAS into an operational field measurement system. This was done in cooperation with the Swiss applied sciences institute NTB (Buchs, SG, Switzerland). The focus was the design of a simple, reliable instrument optimised for measurement cam-

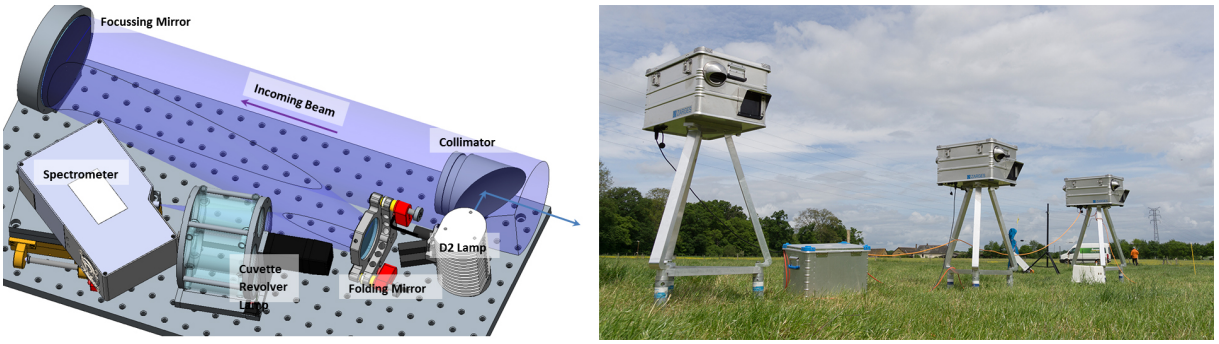

Figure 1. Swiss miniDOAS scheme and field set-up of three instruments (retro-reflectors and shutter not shown).

paigns in which the miniDOAS can be operated as a stand-alone device.

In this paper we present modifications and additions to the original RIVM model. These include the simplification of the optical arrangement; introduction of another type of light source; a temperature-regulated spectrometer; a revolver for calibration cuvettes; a laser for light source–reflector alignment; a temperature-controlled, weather-resistant housing; and stands for a stable field set-up of instrument and reflector. We describe an advanced DOAS data evaluation that ensures the validity of the concentration calculation over a wide range, and we characterise instrument performance based on inter-comparisons with acid traps as well as parallel miniDOAS measurements. One application example of the new Swiss miniDOAS is the determination of NH_3 emissions from agricultural surfaces. We present miniDOAS measurements resolving small and large vertical and horizontal NH_3 concentration differences, which can be used for emission determination, for example based on inverse dispersion modelling. Highlighted experiments comprise the determination of

- concentration differences and emissions from field application of cattle slurry,
- concentration differences and emissions from a paddock grazed by dairy cattle,
- concentration differences due to the emission from an artificial source along with elevated ambient SO_2 levels caused by the passage of the plume of the Holuhraun eruption of the Icelandic Bárðarbunga volcano in 2014 (Boichu et al., 2016; Gauthier et al., 2015).

2 Material and methods

2.1 The Swiss miniDOAS instrument

Figure 1 shows the main optical components of the Swiss miniDOAS version. The light source is a deuterium lamp (D2; Hamamatsu) in which the light is deflected 90° and collimated by an off-axis parabolic mirror (EdmundOptics, custom-coated with an Al-based VUV–IR mirror coating), and directed to a hollow retro-reflector (Newport UBBR2.5-5UV, not displayed) at a distant location. Returned light is focussed by a parabolic mirror (Edmund Optics, custom-coated with an Al-based VUV–IR mirror coating) and directed into the spectrometer with the possibility for remote-controlled calibration using a custom-tailored revolver equipped with cuvettes containing known amounts of calibration gas. We used gas cells (0.075 m length) with pure N_2, NH_3 (191.9 mg m^{-3}), NO (594.0 mg m^{-3}) and SO_2 (76.3 mg m^{-3}) (those three species in N_2) at a pressure of 963 mbar and a temperature of 298 K. The D2 lamp exhibits superior UV performance, less noise and less visible light, compared to the widely used xenon-type lamp (compare specifications at www.hamamatsu.com). An automated shutter (CVI rotor drive bi-stable flag shutter 04RDS501 with a custom-made USB driver) in front of the spectrometer aperture was implemented for dark spectrum recording. The used spectrometer (OceanOptics QE65PRO; slit width 100 µm, grating #H7) features a thermoelectric temperature control and was operated at −10 °C. A geometric cut-off, achieved by the tuning of the grating, prevents blooming due to high intensities potentially occurring with the spectrometer's charge-coupled device (CCD) array beyond 230 nm. The evaluated wavelength window covers 203.7 to 227.8 nm with 274 × 58 CCD pixels (horizontal × vertically binned). A light beam adjustment using piezo motors (Newport Picomotor) was implemented at three locations: two motors actuate the folding mirror, and one moves the spectrometer along the optical axis into the "image distance". The instrument is built into a robust, weather-proof, thermally insulated box. A pointing laser parallel to the light beam helps with the set-up of the box-reflector system. The box includes a ventilation system, coupled to the breadboard temperature, keeping instrument temperature constant within a few degrees. Retro-reflectors are installed in a camera housing with heating to prevent condensation on the window or the retro-reflector. We equipped the instrument (as well as the reflector) with a solid, custom-made tripod, where instrument and tripod can

be connected directly into the breadboard. It is possible to mount the tripod on massive soil screws to ensure a stable field set-up (Fig. 1).

In this article, we present measurements from three systems (models N1, N2 and N3). One experiment (E1, Sect. 2.3) includes measurements with an older version (O1) where another spectrometer (Avantes AvaSpec-2048x14 – same as in Volten et al., 2012) had been used and where the box temperature was not controlled. Raw data are recorded by a custom LabView (National Instruments) program, running on a notebook within the instrument. Light level is maximised by automatically adjusting the folding mirror. Alternatively it can be remotely adjusted. Quality parameters and preliminarily calculated concentrations are provided in real time.

2.2 DOAS concentration calculation

The DOAS principle is based on the linearisation of the Lambert–Beer law (Platt and Stutz, 2008):

$$\ln\left(\frac{I(\lambda)}{I_0(\lambda)}\right) L_{\text{path}}^{-1} = \sum\left(-\sigma_i(\lambda)\, c_i\right) + P(\lambda), \tag{1}$$

where I_0 denotes the initial intensity of the light beam emitted by the light source and I is the radiation intensity of the beam after passing through a layer of thickness L_{path} (i.e. I represents a typical measurement spectrum); λ represents wavelength, i the index for a specific trace gas (here: NH_3, NO, SO_2), σ_i the absorption cross section (of trace gas i with narrow-band absorption features), c_i the trace gas amount and P the spectral broadband structures. For simplicity, we skip the display of λ in the following.

The crucial step of the DOAS data evaluation is the distinction between broadband effects P and narrow-band absorption structures in σ_i. This is accomplished by spectral high-pass filtering while retaining the narrow-band features of σ_i (Platt and Stutz, 2008).

We call the miniDOAS measurement spectra I_{meas}(e.g. provided as 1 min mean). Each I_{meas} is corrected for the spectrometer background signal – a "dark spectrum" (I_{dark}) – recorded with blocked spectrometer inlet (Eq. 2). Pixels at the far end of the CCD, where no light should be received by the grating, are used to map the influence of stray light (I_{stray}) within the detector cell. I_{stray} is assumed to show a uniform distribution across the CCD array, and this offset is considered for each spectrum for further calculations (Eq. 2).

$$I_{\text{adj}} = I_{\text{meas}} - I_{\text{dark}} - I_{\text{stray}} \tag{2}$$

The first step in the evaluation is the improvement of the signal-to-noise ratio by dividing the measured spectrum I_{adj} by a reference spectrum I_{ref}. $\frac{I_{\text{adj}}}{I_{\text{ref}}}$ will be called I_{div}.

Following Eq. (1) we define

$$\ln(I_{\text{div}})\, L_{\text{meas}}^{-1} = \sum\left(-\sigma_i\left(C_i - \frac{L_{\text{ref}}}{L_{\text{meas}}} c_{\text{ref},i}\right)\right) + \hat{P} = \sum\left(-\sigma_i \hat{c}_i\right) + \hat{P}, \tag{3}$$

where

$$C_i = \hat{c}_i + \frac{L_{\text{ref}}}{L_{\text{meas}}} c_{\text{ref},i} \tag{4}$$

is the path-averaged, absolute concentration over the measurement path length L_{meas}. L_{ref} is the measurement path length representative for I_{ref}. $\hat{c}_i$ is the concentration difference of species i to the concentration associated with the (path-adjusted) reference spectrum $c_{\text{ref},i}$. $\hat{c}_i$ can be positive or negative, depending on the magnitude of $c_{\text{ref},i}$. $\hat{P}$ is the residual broadband structure. We arbitrarily define I_{ref} as the time average of I_{adj} during a confined period, which could ideally be assumed to be representative for the measurement situation. I_{ref} will contain absorption from unknown amounts of the target trace gases $c_{\text{ref},i}$ present at the averaging time. Once that $c_{\text{ref},i}$ has been quantified, $\hat{c}_i$ can be corrected posteriori (Eq. 4).

Various ways to estimate $c_{\text{ref},i}$ are discussed in Sect. 3.2.3. One approach, chosen here, consists of inter-comparison measurements with other systems, such as alpha passive samplers for NH_3 (Tang et al., 2001) distributed along L_{path}.

In order to eliminate $\hat{P}$, a high-pass filter (indicated by $\{\dots\}$), optimised to account for the shape of $\hat{P}$, is applied to all spectra, resulting in

$$\ln(\{I_{\text{div}}\})\, L_{\text{meas}}^{-1} = \sum(\{-\sigma_i\}\,\hat{c}_i). \tag{5}$$

$\{-\sigma_i\}$ are henceforth termed differential absorption cross sections Θ_i. For the determination of $\hat{c}_i$, Θ_i are fitted to the measured "differential optical depth" $D = \ln(\{I_{\text{div}}\})$ by multiple linear regression.

The Θ_i used for our evaluation (Fig. 2b) were obtained by calibration with a flow cuvette, similar to Volten et al. (2012). Calibration spectra are treated exactly the same way as the regular measurement spectra. The uncertainty of $\hat{c}_i$ is given by the corresponding standard error (SE_i) as a result from the multiple linear fit (Stutz and Platt, 1996).

In practice, the applied DOAS routine is similar to that used by Volten et al. (2012). However, the concentration calculation was further adapted to meet our requirements for a robust and efficient high-pass filtering of I_{div} and linear response over a wide ambient concentration range. For high-pass filtering we employ local regression (Cleveland et al., 1988; Jacoby, 2000) by using a combination of local polynomial regression ("loess" method: R Core Team, 2016) and robust extraction of baseline signals (REBS: Ruckstuhl et al., 2012; "rfbaseline" method: R Core Team, 2016) in order to achieve low-pass filtering as a basis for the high-pass filter. The alpha parameter defines the running window used for local regression as a fraction of all investigated CCD pixels.

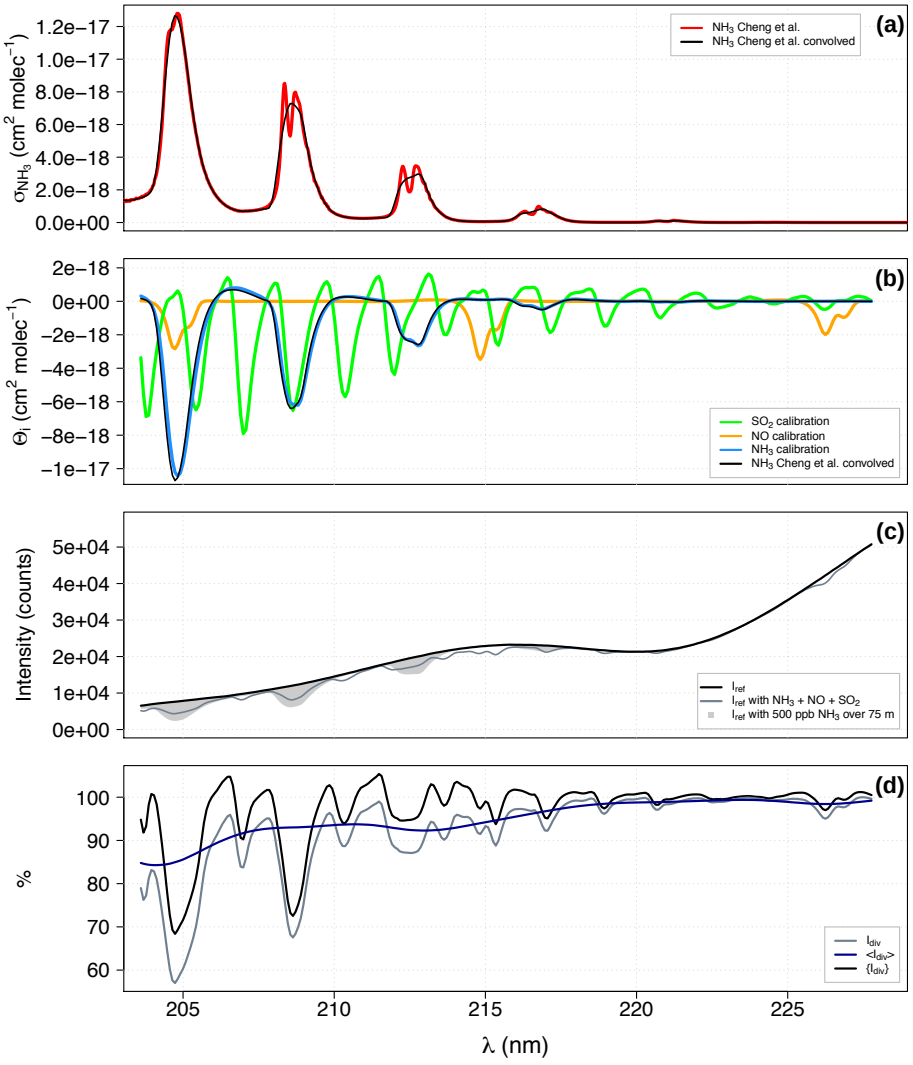

Figure 2. miniDOAS calibration-derived differential absorption cross sections Θ_i and literature-derived absorption cross section σ_{NH_3}, including example data evaluation steps; **(a)** σ_{NH_3} by Cheng et al. (2006) including convolution to the CCD pixel resolution, **(b)** Θ_i (obtained from $\{I_{div}\}$ by instrument N2 calibration, performed with cuvette concentrations of 191.9 mg NH_3 m^{-3}, 76.3 mg SO_2 m^{-3}, 594.0 mg NO m^{-3}) and compared to the literature values for NH_3 as shown in **(a)**, **(c)** spectrum I_{ref} and I_{adj} including simulated absorption by NH_3 alone and all three gas species combined and **(d)** different evaluation steps for I_{div} using the combined spectrum from **(c)**.

REBS is based on robust local regression with asymmetric outlier weighing in order to extract the baseline signal from a series of data points (Ruckstuhl et al., 2012). For low-pass filtering, a smoothed (loess, alpha = 0.15) REBS baseline (rf-baseline, alpha = 0.13) of I_{div} is derived:

$$\langle I_{div} \rangle = \text{loess}(\text{REBS}(I_{div})), \quad (6)$$

where $\langle \dots \rangle$ indicates low-pass filtering. For high-pass filtering the step is iterated a second time (loess, alpha = 0.2) so that

$$\{I_{div}\} = \frac{I_{div} \langle I_{div} \rangle^{-1}}{\langle I_{div} \langle I_{div} \rangle^{-1} \rangle}. \quad (7)$$

When fitting Θ_i by ordinary least-square (OLS) regression, often some degree of autocorrelation is visible in the residual spectrum. Concentrations estimated with such properties are biased and resulting SE_i can be too small (Platt and Stutz, 2008). In order better account for autocorrelation, we include terms of an autoregressive moving-average (ARMA) regression model (Brockwell and Davis, 2002; R Core Team, 2016) in our fitting procedure. The terms of the ARMA models are allowed to contain only up to two orders, resulting in a total of five parameter combinations. The best model for each spectrum is selected using the corrected Akaike information criterion (Brockwell and Davis, 2002). Volten et al. (2012) consider potential wavelength drift with the detector by searching for the best correlation of the DOAS fit

Table 1. Overview of experimental trials as examples for miniDOAS applications.

Experiment:	E1	E2	E3	E4	E5
Site	Witzwil, CH; 46°59′06″ N, 7°04'32″ E, grassland	Witzwil, CH; 46°59′06″ N, 7°04'32″ E, grassland with dead canopy	Rennes, FR; 48°07′02″ N, 1°47'50"E, paddock before grazing	Rennes, FR; 48°07′02″ N, 1°47'50"E, paddock during grazing	Auditorium of HAFL closed room with passive ventilation
Measurement period	01/09–02/09/2014	22/09/2014	07/05/–11/05/2015	18/05/–19/05/2015	11/06/–12/06/2015
Subject of investigation	NH_3 emissions from cattle slurry application	NH_3 emissions from release grid; Bárðarbunga SO_2 plume	miniDOAS concentration inter-comparison	NH_3 emissions from paddock grazed by dairy cattle	miniDOAS & impinger inter-comparison at a high concentration level
Approach	Horizontal concentration differences + bLS & IHF	Horizontal & vertical concentration differences+ bLS & mass balance method	miniDOAS & alpha samplers	Horizontal concentration differences + bLS	12 impingers parallel on miniDOAS path
DOAS systems used	O1, N1	N1, N2, N3	N1, N2	N1, N2	N1, N2
L_{path} (m)	80	72.6/ 73.6/ 76.4	75.4	75.4	57.5
Measurement height (m)	1.25	0.49, 1.25, 3.01	1.25	1.25	1.25

when shifting over the CCD array. Since we use a thermo-electrically cooled spectrometer, which does not show major systematic CCD pixel drift, we restrict this step to shifts of ± 1 pixel.

2.3 Field experiments

As a demonstration of applications for the miniDOAS instrument, exemplary results obtained from five experiments with a focus on NH_3 are presented (Table 1). Two experiments (E3 and E5) focused on inter-comparisons. During E3, two miniDOAS systems were operated in parallel. At the E5 trial, the same systems were inter-compared to impinger NH_3 measurements. With E1, E2 and E4 horizontal and vertical concentration differences are presented. These experiments investigated NH_3 gradients related to emissions from slurry application (E1) and from an artificial NH_3 source (E2) as well as from a paddock grazed by dairy cattle (E4). These concentration differences can be used to determine the associated NH_3 emissions by means of inverse dispersion models, such as with backward Lagrangian stochastic (bLS; Flesch et al., 2004) dispersion modelling (e.g. "WindTrax", www.thunderbeachscientific.com) or with the "FIDES" model (Loubet et al., 2010). In the following the experimental set-ups are briefly outlined.

2.3.1 Inter-comparison with impingers

A comparison between wet-chemical impingers and the miniDOAS was performed indoors in the auditorium of the agricultural school HAFL in Zollikofen, Switzerland (trial E5). The NH_3 concentrations were modulated by ventilation that is scaled with the CO_2 concentration in the room and is switched of during night-time. Two miniDOAS systems were placed in the diagonal of the room with a path length of 57.5 m. Twelve impingers, similar to those presented by Häni et al. (2016), were evenly distributed on both sides along the miniDOAS beams.

2.3.2 Parallel miniDOAS measurements and NH_3 emissions from grazing cattle

The French programme BTéP (Emissions gazeuses au Bâtiment, sTockage, Epandage et Pâturage des systèmes bovins laitiers) is devoted to investigating NH_3 emissions along the production chain of a dairy system. One aspect was the determination of NH_3 emissions during grazing. Measurements took place in May 2015 at the "Institut de l'Elevage" Monvoisin – BP 85225 35652 Le Rheu Cedex, Brittany in France. Before the grazing period the miniDOAS systems were run side by side (experiment E3) and run in parallel with alpha passive samplers (Tang et al., 2001). Three alpha sampler

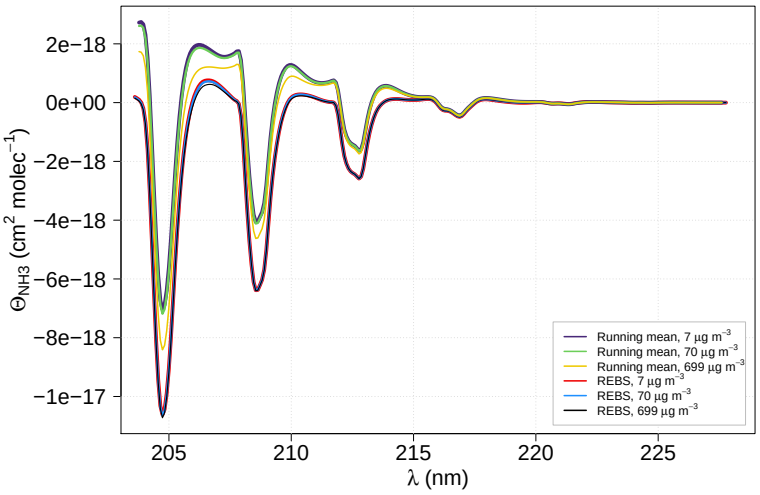

Figure 3. Θ_{NH_3} derived from simulated I_{adj} with absorption from $\hat{c}_i = 7$, 70 and 699 µg NH_3 m^{-3} over $L_{path} = 75$ m; two types of high-pass filters are investigated: one based on a running mean over a 27-pixel window (≈ 7.7 % of investigated wavelength range, similar to Volten et al., 2012) and one based on our REBS filter.

batches (i.e. replicates of three samplers) were distributed evenly along the miniDOAS path. To estimate NH_3 emissions under grazing conditions, the miniDOAS systems were located up- and downwind at the edges of the grazed paddock of about 0.5 ha (Fig. S1 in the Supplement) with a path length of 75.4 m. We tentatively calculated NH_3 emissions based on bLS and miniDOAS. Details about the used bLS approach are documented by Häni et al. (2016).

2.3.3 Emissions from slurry field application

The site Witzwil (46°59′06″ N, 7°04′32″ E) is located on the Swiss Plateau 431 m a.s.l. The experiment took place on a 18 ha flat grassland field that was cut at the end of August and treated with glyphosate on 6 September 2014 to prepare a no-till sowing. On 1 September 14:00 cattle slurry was applied to a circular plot with a radius of 19 m (Fig. S2). Moderate easterly winds prevailed. The miniDOAS O1 was placed east of the circle to monitor the inflow NH_3 concentration, and N2 was placed 5 m downwind of the circle. For comparison, NH_3 emissions were derived from bLS–impinger measurements as well as from an integrated horizontal flux (IHF) approach (Denmead, 1995) with impinger measurements on a vertical profile at the plot centre. Details about these methods and the experiment can be found in Häni et al. (2016).

2.3.4 Artificial gas release

On 22 September an artificial gas release source was installed on the dead grass canopy at Witzwil. The source consisted of a grid of 36 critical orifices (100 µm diameter, stainless steel, LenoxLaser, USA) in order to release gas at a known mass-flow rate. The grid was designed to approximate a circular area with a radius of 10 m, i.e. an area of 314 m^2 (see Fig. S3). The orifices were placed equidistant to each other and were radially connected to a distribution unit at the centre with eight 6 mm (OD) PA (Legris, Parker Hannifin) tubes. Gas supply was regulated by a mass-flow controller (red-y smart controller, Voegtlin Instruments, Switzerland). Grid pressure was monitored to guarantee constant overpressure. 4.97 % NH_3 in N_2 gas standard (5.0, CarbaGas, CH) was used with a release rate of 10 standard L min^{-1}, corresponding to an average emission rate of 6.281 mg s^{-1} over a circular area with a radius of 10 m. For this experiment we used three miniDOAS systems (N1, N2, N3), placed downwind of the source at a distance of 3 m from the edge of the source. The heights of the three systems were 0.49, 1.25 and 3.01 m above ground, with L_{path} between 72 and 76 m.

3 Results and discussion

3.1 Differential absorption cross sections

The NH_3 absorption cross section by Cheng et al. (2006) (from the UV/VIS Spectral Atlas; Keller-Rudek et al., 2013) was compared to Θ_{NH_3} from our calibration after convolution of the literature values to the spectrometer's CCD resolution (Fig. 2a). Calibrations were within ±3 % of the differential absorption cross section derived from Cheng et al. (2006) (Fig. 2b and Sect. 3.2.3). This value reflects the uncertainty of our Θ_{NH_3}.

Figure 2c shows I_{ref} and I_{adj} with absorption by NH_3, NO and SO_2. The applied high-pass filter represents a baseline to narrow-band absorption (Fig. 2d). This is individually shown for NH_3, NO and SO_2 in Fig. 2b, as well as for all three gases combined. As a result, Θ_i are independent from the magnitude of absorption (or the ambient concentration for a given L_{path}) (Fig. 3). For verification, $\{I_{div}\}$ was calculated

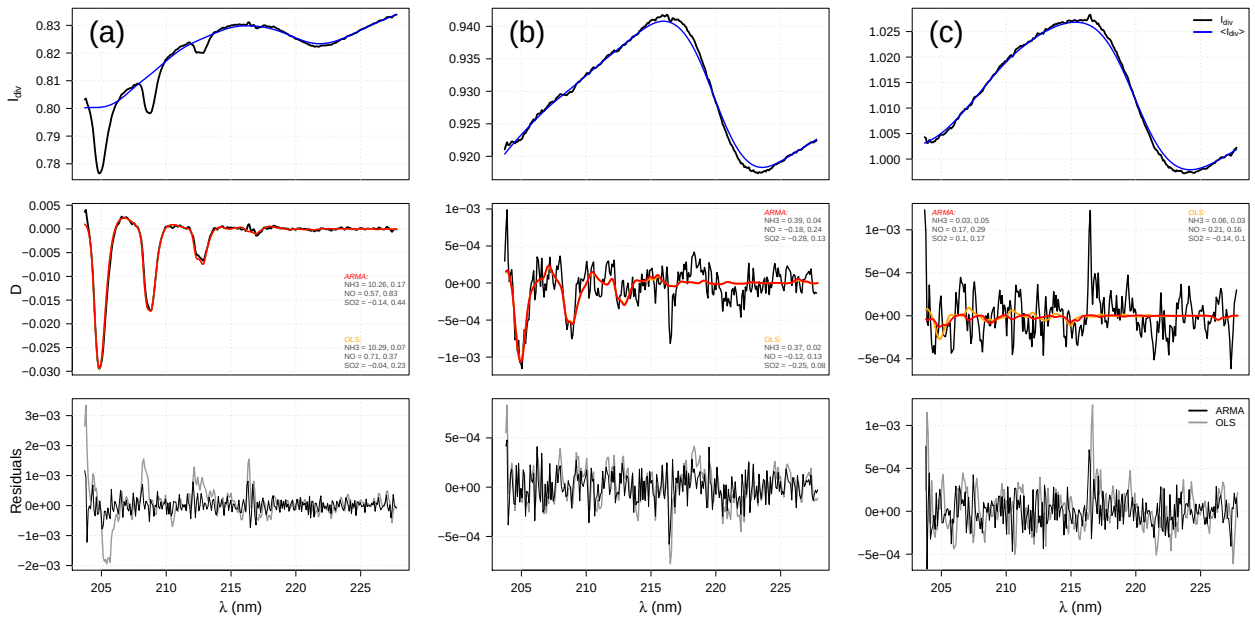

Figure 4. Spectra from concentration evaluation for three cases: **(a)** a relatively high ($\hat{c}_{NH_3} = 10.26\,\mu g\,m^{-3}$), **(b)** a small ($\hat{c}_{NH_3} = 0.39\,\mu g\,m^{-3}$) and **(c)** a $\hat{c}_{NH_3}$ value close to zero; three different evaluation steps are shown: I_{div}, differential optical depth D and residual spectrum; the difference between ARMA regression and OLS regression is also highlighted; residuals from the OLS fit exhibit significant degrees of autocorrelation down to lags of 7, 5 and 4 pixels, for cases **(a)**, **(b)** and **(c)**, respectively, whereas the ARMA model fit successfully considered this autocorrelation.

for NH_3 with simulated spectra using the absorption cross section by Cheng et al. (2006), based on ambient concentrations of 7, 70 and 699 $\mu g\,m^{-3}$ across $L_{path} = 75$ m. Resulting Θ_{NH_3}, evaluated with the REBS high-pass filter, were equivalent over the entire concentration range, demonstrating that the procedure provides robust results over a wide range of ambient concentrations (Fig. 3). For comparison, a running-mean-based high-pass filter yields Θ_{NH_3} that slightly depend on the amount of absorption. The deviations are non-linear and will depend on the moving average filter's parameters (such as the width of the running window). They are in the order of up to 3 % over the analysed concentration range.

The REBS method (Sect. 2.2) is conducted with one-sided outlier weighting. Situations resulting in apparent negative concentrations (meaning I_{adj} exhibits less narrow-band absorption than I_{ref}) are assessed this way with a higher uncertainty. Consequently, using the REBS-based low-pass requires that I_{ref} is ideally taken during periods with the lowest expected concentrations by all three gases. The R script used to evaluate the concentrations is given in the Supplement.

3.2 Instrument performance

3.2.1 Field operation

Within a range of ambient air temperatures between −10 and 30 °C, the temperature inside the miniDOAS box can be kept constant (here at 35 °C) within 3 °C, while the spectrometer keeps its temperature set to −10 °C. Feasible L_{path} range between 10 and 100 m as the optical arrangement limits the minimum reflector distance, whereas light loss due to increasing beam diameter and O_2/O_3 absorption restricts the maximum distance. The usual spectrometer integration time for a single spectrum is between 20 and 150 ms. With the stable mounting of instrument and reflector, measurement uptime close to 100 % is possible and is primarily limited by fog episodes.

3.2.2 Filters and multiple linear fit

Figure 4 demonstrates the presence of non-random noise structures in I_{div}. I_{div} experiences broadband deformation $\hat{P}$ to various degrees (in the order of a few per cent at maximum), changing on timescales of hours to days. This can be caused by Rayleigh and Mie extinction, broadband-like absorption by gases and further detrimental instrumental effects such as unevenly distributed stray light within the spectrometer cell. Depending on the interaction of the low-pass filter with unfavourable combinations of strong $\hat{P}$ deformation and noise might lead to autocorrelation structures in the residual spectrum. Figure 4 demonstrates three different cases with the focus on NH_3 in order to highlight features and limitations of the concentration calculation. Small differences between $\hat{c}_{NH_3}$ and associated SE_{NH_3} from the ARMA and an OLS fit, respectively, become evident. We regard the advantage of the applied ARMA model over the OLS regression

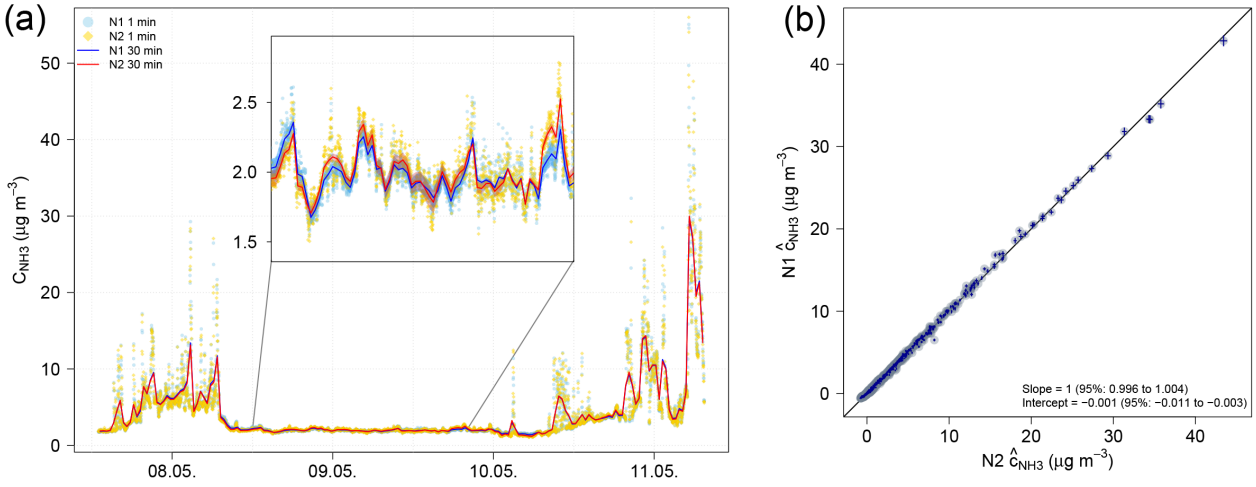

Figure 5. Concentration inter-comparison of two miniDOAS instruments (N1, N2) operated in parallel during experiment E3; **(a)** time series ($c_{\mathrm{ref,\,NH_3}} = 1.92\,\mu\mathrm{g\,m^{-3}}$ was added, determined by parallel measurements with three alpha sampler batches, distributed along the miniDOAS path; shaded areas show the $\mathrm{SE_{NH_3}}$ range for 30 min time resolution), **(b)** regression (Deming method; Linnet, 1990) of 5 min averages ($n = 1086$; without $c_{\mathrm{ref,\,NH_3}}$); slope and intercept are given with 95 % confidence interval limits; crosses in the scatter plot reflect the range of $\hat{c}_{\mathrm{NH_3}} \pm \mathrm{SE_{NH_3}}$).

as twofold: first, autocorrelation structures in the residual spectrum can impose features resulting in artefact concentration values when using the OLS regression. ARMA regression yields more robust results for all three gases. Second, SE_i, as a result of the ARMA fit, tends to be larger than that from OLS and better approximates the fit's uncertainty. We checked potential interference by rotating sealed cuvettes (N_2, NH_3, NO, SO_2) into the beams of two instruments. The largest effect was observed from SO_2 on NO with up to −15 % (based on molecular number densities). The effect of SO_2 on NH_3 was at most −2 %. An example is given in the Supplement (Table S1). Results differ between instruments and depend upon the used I_{ref}.

Interferences are also visible in the increased standard errors (SE_i) in Table S1.

3.2.3 miniDOAS inter-comparison

During experiment E3 two miniDOAS models (N1 and N2) were operated in parallel under identical conditions for 4 days. Figure 5 shows the time series of $C_{\mathrm{NH_3}}$ and a scatter plot of $\hat{c}_{\mathrm{NH_3}}$ from instruments N1 and N2. For a direct comparison, $\Theta_{\mathrm{NH_3}}$ from individual calibrations were adjusted in order to match the literature-derived cross section (see Sect. 3.1). Applied corrections were −1.3 and 2.5 % for instrument N1 and N2, respectively. The time series was characterised by easterly winds at the beginning and towards the end, where advected NH_3 from a nearby stable produced elevated and fluctuating concentrations. During the period in-between, westerly winds with low and constant concentrations prevailed.

The ranges of SE_i were assessed from 1 min averaged spectra (also see Fig. S4). Median SE_i were 0.06 µg NH_3 m^{-3} (interquartile: 0.05 to 0.09), 0.33 µg NO m^{-3} (0.24 to 0.41) and 0.18 µg SO_2 m^{-3} (0.14 to 0.22). Calculations based on 30 min averaged spectra yielded similar ranges. This suggests that the uncertainty of the $\hat{c}_i$ calculation was influenced by non-random spectral structures. The concentration differences between N1 and N2, evaluated with half-hourly means, were of a similar magnitude to the associated SE_i, demonstrating that SE_i are a suitable measure for the random uncertainty of concentration calculation (Stutz and Platt, 1996). Figure 6 shows the relationship of $\mathrm{SE_{NH_3}}$ to the concentration level. For N2 it was evaluated to 0.8 %, whereas for N1 it was 1.4 % of the concentration. This indicates that the uncertainty of $\hat{c}_{\mathrm{NH_3}}$ depended on instrumental features.

The NH_3 inter-comparison time series and regression of N1 onto N2 (Fig. 5) reveal the consistency between both instruments, which further consolidates the uncertainty analysis. The instruments show very good agreement with only minor deviations caused by episodes of drift between both instruments. The slope of N1 onto N2 is one, and the intercept is close to zero. Overall, the NH_3 limit of detection (LOD) against c_{ref} for 1 to 30 min concentrations, approximated as 3 times the median $\mathrm{SE_{NH_3}}$, is 0.2 µg m^{-3}. In general, we determine the system's random uncertainty for NH_3 to be at minimum the LOD or 1.4 % of $\hat{c}_{\mathrm{NH_3}}$ (Fig. 6).

The exact determination of $c_{\mathrm{ref},\,i}$ is a challenge. Measurement inter-comparisons with other systems can constrain $c_{\mathrm{ref},\,i}$. As such comparison systems are mostly point-location measurements, it is necessary that horizontal concentration gradients are small within the miniDOAS path

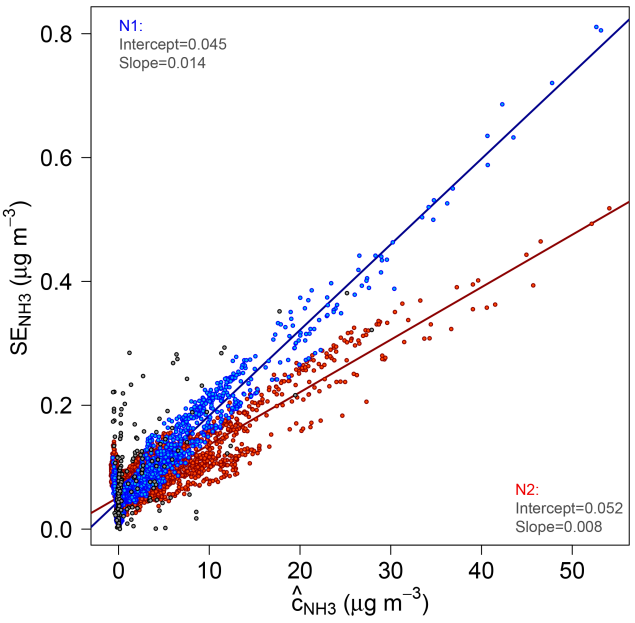

Figure 6. SE_{NH_3} vs. $\hat{c}_{NH_3}$ (instruments N1 and N2); coloured circles represent 1 min averages, and grey circles display the difference in concentration determined by instrument N1 and N2 for half-hourly means ($\Delta_{30} = |N1-N2|$) of the individual 1 min values; regression was carried out with the Deming method (Linnet, 1990).

and are representatively caught by the point measurements. For the results presented in Fig. 5, $c_{ref,\,NH_3} = 1.92\,\mu g\,m^{-3}$ was derived from parallel measurements with three alpha sampler batches distributed along L_{path}. The coefficient of variation of the alpha samplers was 4.5 % or $0.09\,\mu g\,m^{-3}$. Hence, we expect the uncertainty of $c_{ref,\,NH_3}$ to be about $2 \times 0.09\,\mu g\,m^{-3} \approx 0.2\,\mu g\,m^{-3}$. This effect in $c_{ref,\,NH_3}$ will contribute systematically to the overall uncertainty in C_{NH_3}, since it persists systematically as long as a specific I_{ref} is used. In principle, there are alternative ways to approximate $c_{ref,\,NH_3}$ as follows:

a. During long-term concentration monitoring, periods with lowest ambient concentrations reflect conditions closest to zero. For example, NH_3 can be very low during or after rainfall and under cool temperatures and in a well-mixed boundary layer.

b. I_{ref} could be recorded at very remote places, where it is a safe assumption to find extremely low ambient concentrations. An NH_3-free situation could also be attempted by construction of a "giant denuder" with NH_3 scrubbing, where I_{ref} is recorded within the denuder tunnel.

c. $c_{ref,\,NH_3}$ could be derived by substituting I_{ref} with $<I_{ref}>$for the calculation of I_{div}, thus excluding narrow-band absorption. This can be done using our REBS-based low-pass filtering approach (Sect. 2.2). Since the signal-to-noise ratio in this approach is inevitably larger than with $I_{div} = \frac{I_{adj}}{I_{ref}}$, this approach yields results with higher uncertainty. The absorption present in I_{ref}, used for E3, was analysed using the REBS method to derive a new, synthetic I_{ref} without narrow-band absorption structures. This analysis yielded $c_{ref,\,NH_3} = 1.9\,\mu g\,m^{-3}$ – similar to the inter-comparison with alpha samplers. However, the statistical uncertainty is high ($SE_{NH_3} = 1.35\,\mu g$) and the result is sensitive to the REBS filter width.

The miniDOAS determines SO_2 and NO besides NH_3; the system is optimised for the latter. SO_2 and NO absorption signatures are considered, and their c_{ref} does not have to be known for an accurate NH_3 determination. $c_{ref,\,i}$ represents a constant reflecting the ambient concentration during I_{ref} definition. It does not affect the linearity or random uncertainty of the calculation. In the case of NH_3, $c_{ref,\,NH_3}$ from any of the discussed approaches is expected to be accurate at best by $0.2\,\mu g\,m^{-3}$, which represents the absolute limit to overall uncertainty.

3.2.4 Concentration inter-comparison

The miniDOAS systems (N1 and N2) have been compared to conventional impinger systems in an indoor experiment (E5, Sect. 2.3). The two systems were independently calibrated, which allows for an independent comparison of the concentrations (Table 2). For the impinger results the uncertainty range is indicated as the standard error of the mean value. The miniDOAS uncertainty of the average C_{NH_3} is indicated as the standard deviation of the 1 min values during the corresponding intervals. As the reference spectra from the BTéP campaign were used, an offset of $c_{ref\,NH_3} = 2.5\,\mu g\,m^{-3}$ was added to $\hat{c}_{NH_3}$. The measurements in the HAFL auditorium showed small differences between miniDOAS and impingers. These were smaller than the uncertainty between both systems (10 %) when the ventilation of the room was switched off after 18:00. The first two intervals showed larger differences, but they were within the uncertainty of the measurements. However, they might reflect the existing inhomogeneity of the concentration field in the room.

3.3 Ammonia field experiments

3.3.1 Concentration differences due to grazing cattle

From 13 to 19 May 2015 miniDOAS N1 was located at the SW side of the field, and N2 in the centre (Fig. S1). Twenty-six cows grazed the SW quarter of the field from the morning of 18 May until early afternoon on 19 May. As the wind direction during this period tended to be between SW and WNW, N1 represented the inflow concentration and N2 measured an outflow concentration influenced by the NH_3 emission caused by the cows grazing on the pasture. A systematic increase of the horizontal concentration difference, from the beginning of grazing until the early afternoon the

Table 2. NH_3 concentration comparison between impinger systems and the miniDOAS systems N1 and N2 at the HAFL auditorium.

Time	Impinger ($\mu g\,m^{-3}$)	Impinger standard error ($\mu g\,m^{-3}$)	miniDOAS (C_{NH_3}, mean value N1 & N2) ($\mu g\,m^{-3}$)	miniDOAS standard deviation ($\mu g\,m^{-3}$)
11/06/15, 12:30–16:00	75.0	6.6	72.0	8.6
11/06/15, 16:00–18:00	77.9	4.7	74.2	6.7
11/06/15, 18:00–20:00	84.0	2.4	84.5	6.8
11/06/15, 20:00–22:00	91.7	2.2	94.7	2.5
11/06/15, 22:00–24:00	97.0	1.6	98.4	1.1
12/06/15, 00:00–02:00	98.7	1.8	100.2	0.8
12/06/15, 02:00–04:00	101.5	2.7	103.6	1.2

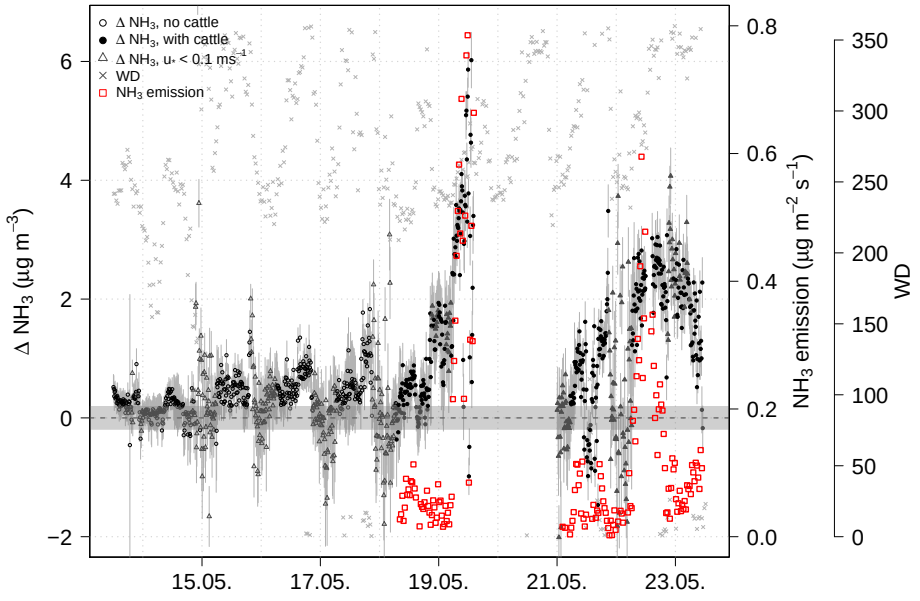

Figure 7. Horizontal NH_3 concentration differences and derived emissions from grazing experiment E4 (Table 1); black/grey open symbols show the period without cattle on the investigated pasture, black/grey filled symbols highlight the period with cattle grazing on subplot or the entire field (see Fig. S1), and red symbols show emissions; concentrations were calculated like in experiment E3; concentration difference uncertainty range (grey lines) represents the maximum limit of 95 % confidence. The grey band indicates $0 \pm 0.2\,\mu g\,m^{-3}$ (LOD); the data gap was caused by power supply interruption and translocation of instrument.

next day (when the miniDOAS systems were moved), was recorded (Fig. 7). This difference, caused by emissions, increased from below the LOD up to $6\,\mu g\,m^{-3}$. From 21 May 2015 onwards, N1 was located at the NW edge, and N2 at the SE border of the entire field, while the cattle grazed at the entire paddock. Again, elevated emission concentration differences were observed. During the period before grazing (13 to 18 May), smaller differences were present probably due to a combination of NH_3 advection from surrounding sources and deposition over the investigated field. We used the concentration differences for a preliminary emission calculation by bLS when the cattle were on pasture. The emissions were generally below $1\,\mu g\,m^{-2}\,s^{-.1}$. They peaked characteristically when the wind blew from a direction where the downwind miniDOAS had a larger concentration footprint within the grazed area, showing that the determination of small emissions with the miniDOAS from grazed systems is possible. A more detailed analysis of these structures, including a more comprehensive estimation of NH_3 emissions due to the excrements of the grazing cows, is beyond the scope of this paper.

3.3.2 Concentration differences and emissions after slurry field application

During the Witzwil experiment (E1), the miniDOAS (N1 and O1) was employed to measure horizontal NH_3 gradients following the application of cattle slurry to an experimental plot of $1250\,m^2$. Application of slurry causes strong

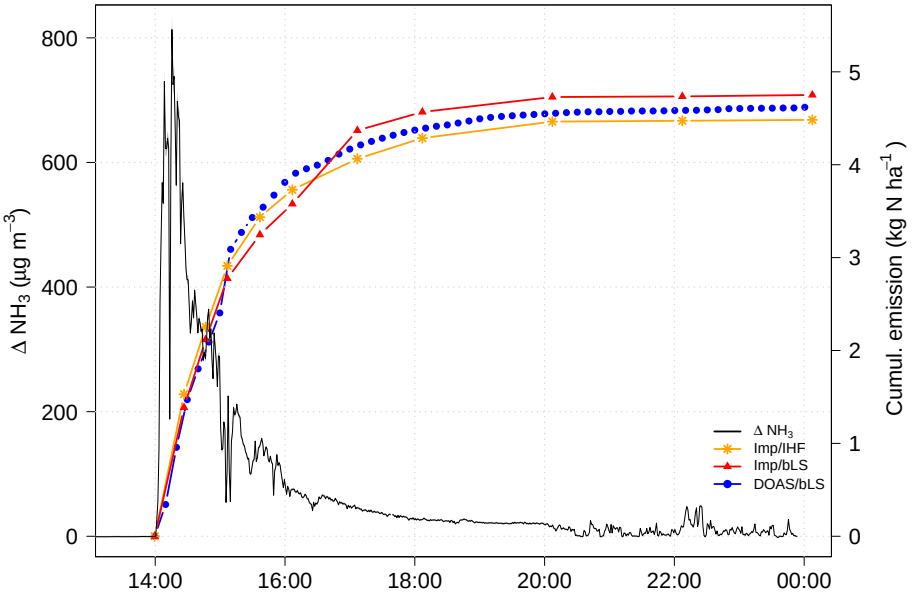

Figure 8. Horizontal NH_3 concentration differences measured by the miniDOAS and cumulated NH_3 emissions (coloured) caused by slurry application to grassland (E1, Table 1); emissions were determined by miniDOAS–bLS and impinger–bLS as well as impinger–IHF (see Sect. 2.4 and Häni et al., 2016); concentration difference uncertainty range (grey) represents the upper limit of 95 % confidence. Note that these values were determined based on turbulence data from a Gill WindMaster Pro ultrasonic anemometer that has a systematic bias in the vertical wind components (see www.gillinstruments.com; Key Note Series Number: KN1509v3) that was not corrected. Considering the correction increases the cumulated emission by ca. 5 %.

emission peaks that typically decrease with half times from less than one to several hours (Häni et al., 2016; Sintermann et al., 2011a; Sommer et al., 2003). Figure 8 shows the horizontal gradients developing between the up- and downwind miniDOAS. The corresponding concentration difference was elevated by up to 800 µg m^{-3} (1 min averages), featuring the characteristic quick decline approximated by a bi-exponential decay over time (Sintermann et al., 2011a). The gradients were used for emission determination based on inverse dispersion modelling with a bLS model (Flesch et al., 2004). Cumulated emissions compare excellently with those derived from impinger concentration measurements in conjunction with bLS as well as with the IHF approach. Details of this experiment are described in Häni et al. (2016).

3.3.3 Artificial source and volcano plume

As part of the trials at the Witzwil site, the emission of an artificial NH_3 source of 20 m diameter was measured with three miniDOAS systems: three instruments (N1, N2 and N3) were put downwind in a vertical profile (E2, Sect. 2.3). The extraordinary and unplanned passage of a huge SO_2 plume, caused by the eruption of the Icelandic Bárðarbunga volcano (Boichu et al., 2016; Gauthier et al., 2015; Umweltbundesamt, 2014), occurred at the same time as the artificial source was in operation. The SO_2 concentrations measured by the miniDOAS agreed well with those recorded by the monitoring stations of the Swiss National Air Pollution Monitoring Network (Fig. 9). The time shift between different stations reflects the passage of the plume over Switzerland. This is indirect evidence that the SO_2 calibration of the miniDOAS system was reliable.

Figure 9 shows the concentrations of NH_3 and SO_2 until 10:00, the period of 22 September before the SO_2 plume arrived. During this period only two systems were in operation. The NH_3 concentrations show an emission profile. Figure 9 also shows the passage of the SO_2 plume combined with the artificial release of NH_3. The release caused a strong concentration difference, whereas the SO_2 concentrations were equal within the associated uncertainty but indicated an expected deposition profile during the plume's passage.

This episode provides an additional field test for cross interference between NH_3 and SO_2. Figure 9 demonstrates how the determination of NH_3 and SO_2 does not interfere with one another. While NO seemed to show no apparent vertical emission or deposition profile, it looks like deviations in the NO signal between instruments and over time occurred primarily due to the presence of large amounts of SO_2. Also, a slight interference of NH_3 on NO was observed for one of the three instruments, consistent with the findings presented in Sect. 3.2.2. The SE_i ranges, however, reflected this uncertainty.

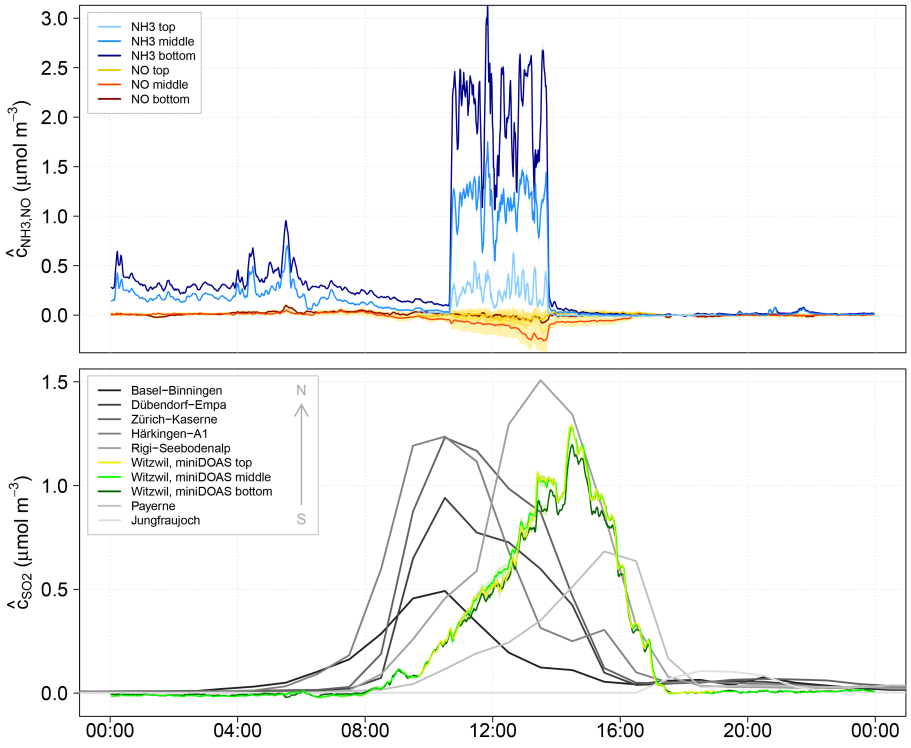

Figure 9. Episode of concentrations $\hat{c}_{NH_3}$, $\hat{c}_{NO}$ and $\hat{c}_{SO_2}$ during the NH_3 gas release experiment (E2, Table 1) coinciding with a SO_2 peak due to the passage of the plume from the Icelandic Bárðarbunga volcano (Boichu et al., 2016; Gauthier et al., 2015; Umweltbundesamt, 2014); miniDOAS concentrations $\hat{c}_i$ (coloured) are shown as 5 min running mean $\pm$ SE$_i$ (data gaps from the topmost miniDOAS instrument result from low light due to software crashes); in grey, concentrations are shown from the Swiss Air Quality Monitoring Network (www.empa.ch/web/s503/nabel).

4 Conclusions and outlook

We have presented a further development of the miniDOAS by Volten et al. (2012) into a stand-alone, field-applicable system for NH_3 measurements, combined with NO and SO_2 determination. Furthermore, we developed a DOAS data evaluation procedure involving local regression, REBS and fitting with an ARMA regression model. This guarantees the linearity of the spectral evaluation over a wide concentration range. The instrument and its performance have been tested and evaluated in field campaigns. This miniDOAS can be used for a wide range of trials, such as flux measurements with approaches based upon horizontal or vertical concentration differences. We have highlighted examples of miniDOAS application for such trials. The involved micrometeorological flux methods can comprise mass balance, aerodynamic gradient (see Wichink Kruit et al., 2010) and inverse dispersion modelling techniques (e.g. this study). The fact that the miniDOAS determines SO_2 and NO alongside NH_3 might be used in emission studies relying on the tracer-ratio method, where NO or SO_2 could be released with known source strength in order to explore the concentration-to-emission relationship and relate that to the miniDOAS NH_3 measurement. The LOD for NO and SO_2 is about 4 times higher than for NH_3 (on a molecular density base). Using an artificial source in a similar way to experiment E2, the release gas concentrations of NO and SO_2 need to be increased from 5 % to about 20 % to get a similar precision to that for NH_3. NO concentrations could often be affected by traffic emissions. The handling of mixing ratios of 20 % NO and SO_2 would need to match safety requirements and cannot be done e.g. in closed rooms.

The concentration differences from 0.28 µg m^{-3} NH_3 (equal to the square root of 2 times the squared LOD of 0.2 µg m^{-3}) up to more than 1000 µg m^{-3} can be resolved, which renders the miniDOAS an exceptionally flexible instrument available for studies investigating strong NH_3 emissions as well as small fluxes. Concentration measurements involving two or more miniDOAS instruments have to be used for flux measurement approaches. Then, the uncertainty of the concentration difference due to spatial gradients is influenced only by the random effect if I_{ref} was defined under identical conditions. The low LOD allows for bi-directional flux monitoring based on the aerodynamic gradient method (Flechard and Fowler, 1998), e.g. over semi-natural and natural ecosystems as long as concentration differences exceed 0.28 µg m^{-3}. One major advantage of the open-path miniDOAS over closed-path systems and filter packs is the

inlet-free, in situ determination of ambient concentrations. This makes the NH_3 measurement insensitive against NH_3 volatilisation from aerosol particles (e.g. at inlet filters) or the interaction of gaseous NH_3 with water molecules and any kind of instrumental surface (Sintermann et al., 2011b, and references therein). The miniDOAS offers full potential for source apportionments where strong NH_3 dynamics have to be considered. Additional instrumental improvements could include an optimisation of the light signal capture – in terms of stability and stray-light minimisation within the spectrometer. A better stray-light performance and higher wavelength pixel resolution over the considered UV window (e.g. using an optimised grating) will further enhance the miniDOAS performance.

The Supplement related to this article is available online at doi:10.5194/amt-9-2721-2016-supplement.

Acknowledgements. We would like to acknowledge Hester Volten, Marty Haaima, Stijn Berkhout and Dan Swaart, all based at RIVM (the Netherlands), for their constructive collaboration providing us with the Dutch miniDOAS prototype and for sharing their knowledge and experience. Also, we thank Chris Fléchard and co-workers for their collaboration and support during the BTéP grazing experiment in Rennes. This project was funded by the Swiss Federal Office of the Environment (contract 06.9115.PZ/L225-3604).

Edited by: C. Brümmer

References

Boichu, M., Chiapello, I., Brogniez, C., Péré, J.-C., Thieuleux, F., Torres, B., Blarel, L., Mortier, A., Podvin, T., Goloub, P., Söhne, N., Clarisse, L., Bauduin, S., Hendrick, F., Theys, N., Van Roozendael, M., and Tanré, D.: Tracking far-range air pollution induced by the 2014–15 Bárdarbunga fissure eruption (Iceland), Atmos. Chem. Phys. Discuss., doi:10.5194/acp-2016-159, in review, 2016.

Brockwell, P. J. and Davis, R. A.: Introduction to time series and forecasting, 2nd ed., Springer, New York, USA, 2002.

Cheng, B., Lu, H., Chen, H., Bahou, M., Lee, Y., Mebel, A. M., Lee, L. C., Liang, M., and Yung, Y. L.: Absorption Cross Sections of NH3 , NH2D, NHD2, and ND3 in the Spectral Range 140–220 nm and Implications for Planetary Isotopic Fractionation, Astrophys. J., 647, 1535–1542, doi:10.1086/505615, 2006.

Cleveland, W. S., Devlin, S. J., and Grosse, E.: Regression by local fitting, J. Econometrics, 37, 87–114, doi:10.1016/0304-4076(88)90077-2, 1988.

Denmead, O. T.: Novel meteorological methods for measuring trace gas fluxes, Philos. T. R. Soc. A, 351, 383–396, 1995.

Edner, H., Ragnarson, P., Spännare, S., and Svanberg, S.: Differential optical absorption spectroscopy (DOAS) system for urban atmospheric pollution monitoring, Appl. Optics, 32, 327–333, doi:10.1364/AO.32.000327, 1993.

Emmenegger, L., Mohn, J., Sigrist, M., Marinov, D., Steinemann, U., Zumsteg, F., and Meier, M.: Measurement of ammonia emissions using various techniques in a comparative tunnel study, Int. J. Environ. Pollut., 22, 326–341, doi:10.1504/IJEP.2004.005547, 2004.

Flechard, C. R. and Fowler, D.: Atmospheric ammonia at a moorland site. II: Long-term surface-atmosphere micrometeorological flux measurements, Q. J. Roy. Meteor. Soc., 124, 759–791, 1998.

Flesch, T. K., Wilson, J. D., Harper, L. A., Crenna, B. P., and Sharpe, R. R.: Deducing ground-to-air emissions from observed trace gas concentrations: A field trial, J. Appl. Meteorol., 43, 487–502, 2004.

Gall, R., Perner, D., and Ladstätter-Weissenmayer, A.: Simultaneous determination of NH_3, SO_2, NO and NO_2 by direct UV-absorption in ambient air, Fresen. J. Anal. Chem., 340, 646–649, doi:10.1007/BF00321528, 1991.

Gauthier, P.-J., Sigmarsson, O., Moune, S., Haddadi, B., and Gouhier, M.: Trace element degassing patterns and volcanic fluxes to the atmosphere during the 2014 Holuhraun eruption, Iceland, in EGU General Assembly Conference Abstracts, vol. 17, p. 10206, 2015.

Häni, C., Sintermann, J., Jocher, M., Kupper, T., and Neftel, A.: Ammonia emission after slurry application to grassland in Switzerland, Atmos. Environ., 125, 92–99, doi:10.1016/j.atmosenv.2015.10.069, 2016.

Jacoby, W. G.: Loess:: a nonparametric, graphical tool for depicting relationships between variables, Elect. Stud., 19, 577–613, 2000.

Keller-Rudek, H., Moortgat, G. K., Sander, R., and Sörensen, R.: The MPI-Mainz UV/VIS Spectral Atlas of Gaseous Molecules of Atmospheric Interest, Earth Syst. Sci. Data, 5, 365–373, doi:10.5194/essd-5-365-2013, 2013.

Linnet, K.: Estimation of the linear relationship between the measurements of two methods with proportional errors, Stat. Med., 9, 1463–1473, doi:10.1002/sim.4780091210, 1990.

Loubet, B., Génermont, S., Ferrara, R., Bedos, G., Decuq, G., Personne, E., Fanucci, O., Durand, B., Rana, G., and Cellier, P.: An inverse model to estimate ammonia emissions from fields, Eur. J. Soil Sci., 61, 793–805, doi:10.1111/j.1365-2389.2010.01268.x, 2010.

Mennen, M. G., Van Elzakker, B. G., Van Putten, E. M., Uiterwijk, J. W., Regts, T. A., Van Hellemond, J., Wyers, G. P., Otjes, R. P., Verhage, A. J. L., Wouters, L. W., Heffels, C. J. G., Romer, F. G., Van Den Beld, L., and Tetteroo, J. E. H.: Evaluation of automatic ammonia monitors for application in an air quality monitoring network, Atmos. Environ., 30, 3239–3256, doi:10.1016/1352-2310(96)00079-9, 1996.

Mount, G., Rumburg, B., Havig, J., Lamb, B., Westberg, H., Yonge, D., Johnson, K., and Kincaid, R.: Measurement of atmospheric ammonia at a dairy using differential optical absorption spectroscopy in the mid-ultraviolet, Atmos. Environ., 36, 1799–1810, doi:10.1016/S1352-2310(02)00158-9, 2002.

Neftel, A., Blatter, A., and Staffelbach, T.: Gas phase measurements of NH3 and NH4 with Differential Optical Absorption Spectroscopy and Gas Stripping Scrubber in combination with Flow Injection Analysis, in: Physico-Chemical Behaviour of Atmospheric Pollutants, edited by: Restelli, G. and Angeletti, G., 83–91, Springer, Dordrecht, the Netherlands, available at: http://www.springerlink.com/index/10.1007/978-94-009-0567-2_13 (last access: 30 July 2015), 1990.

Parrish, D. D. and Fehsenfeld, F. C.: Methods for gas-phase measurements of ozone, ozone precursors and aerosol precursors, Atmos. Environ., 34, 1921–1957, 2000.

Platt, U. and Stutz, J.: Differential optical absorption spectroscopy: principles and applications, Springer, Berlin, Germany, 2008.

R Core Team: R: A Language and Environment for Statistical Computing, R Foundation for Statistical Computing, Vienna, Austria, available at: http://www.R-project.org, last access: 18 March 2016.

Ruckstuhl, A. F., Henne, S., Reimann, S., Steinbacher, M., Vollmer, M. K., O'Doherty, S., Buchmann, B., and Hueglin, C.: Robust extraction of baseline signal of atmospheric trace species using local regression, Atmos. Meas. Tech., 5, 2613–2624, doi:10.5194/amt-5-2613-2012, 2012.

Sintermann, J., Ammann, C., Kuhn, U., Spirig, C., Hirschberger, R., Gärtner, A., and Neftel, A.: Determination of field scale ammonia emissions for common slurry spreading practice with two independent methods, Atmos. Meas. Tech., 4, 1821–1840, doi:10.5194/amt-4-1821-2011, 2011a.

Sintermann, J., Spirig, C., Jordan, A., Kuhn, U., Ammann, C., and Neftel, A.: Eddy covariance flux measurements of ammonia by high temperature chemical ionisation mass spectrometry, Atmos. Meas. Tech., 4, 599–616, doi:10.5194/amt-4-599-2011, 2011b.

Sommer, S. G., Génermont, S., Cellier, P., Hutchings, N. J., Olesen, J. E., and Morvan, T.: Processes controlling ammonia emission from livestock slurry in the field, Eur. J. Agron., 19, 465–486, doi:10.1016/S1161-0301(03)00037-6, 2003.

Stutz, J. and Platt, U.: Numerical analysis and estimation of the statistical error of differential optical absorption spectroscopy measurements with least-squares methods, Appl. Optics, 35, 6041–6053, doi:10.1364/AO.35.006041, 1996.

Tang, Y. S., Cape, J. N. and Sutton, M. A.: Development and Types of Passive Samplers for Monitoring Atmospheric NO_2 and NH_3 Concentrations, Sci. World, 1, 513–529, doi:10.1100/tsw.2001.82, 2001.

Umweltbundesamt: Monatsbericht Hintergrundmessnetz Umweltbundesamt – September 2014, Umweltbundesamt GmbH, Vienna, Austria, available at: http://www.umweltbundesamt.at/fileadmin/site/publikationen/REP0465.pdf (last access: 22 September 2015), 2014.

Volten, H., Bergwerff, J. B., Haaima, M., Lolkema, D. E., Berkhout, A. J. C., van der Hoff, G. R., Potma, C. J. M., Wichink Kruit, R. J., van Pul, W. A. J., and Swart, D. P. J.: Two instruments based on differential optical absorption spectroscopy (DOAS) to measure accurate ammonia concentrations in the atmosphere, Atmos. Meas. Tech., 5, 413–427, doi:10.5194/amt-5-413-2012, 2012.

Wichink Kruit, R., Volten, H., Haaima, M., Swart, D. J. P., van Zanten, M. C., and Van Pul, W. A. J.: Ammonia exchange measurements over a corn field in Lelystad, the Netherlands in 2009, National Institute for Public Health and the Environment, Bilthoven, the Netherlands., 2010.